

Contents

1. DC-RF Gun .....2

2. Experimental Conditions .....3

3. Data Collection and Processing .....3

4. Control Experiments .....6

    4.1 Polarization Dependence .....6

    4.2 Fluence Dependence .....7

    4.3 Accumulated Heating .....8

5. Sample Preparation .....9

6. Data Analysis .....10

    6.1 Change of Basis (Unit Cell) .....10

    6.2 Symmetry changes .....11

    6.3Kinematical Electron Diffraction Simulations .....12

    6.4 Orientation Determination .....13

7. Time dependent model, Correlation function, and Optimization.....17

    Appendices .....26

    References .....28

## 1. DC-RF gun

In this work, we employed a hybrid DC-RF electron gun to generate high brightness femtosecond electron bunches. The system was well characterized and described in a recent study<sup>31</sup>. Fig. S1 shows the schematics of our experiment. A 270-nm UV optical pulse strikes a 20 nm thin film gold photocathode from the back side and generates a high density electron bunch, which is quickly accelerated to a kinetic energy of 95 keV. The bunch then traverses a 3 GHz RF cavity located downstream for temporal rebunching. At the temporal focus, we employed grating enhanced ponderomotive scattering<sup>32</sup> to directly measure the temporal IRF (Instrument Response Function) of our instrument.

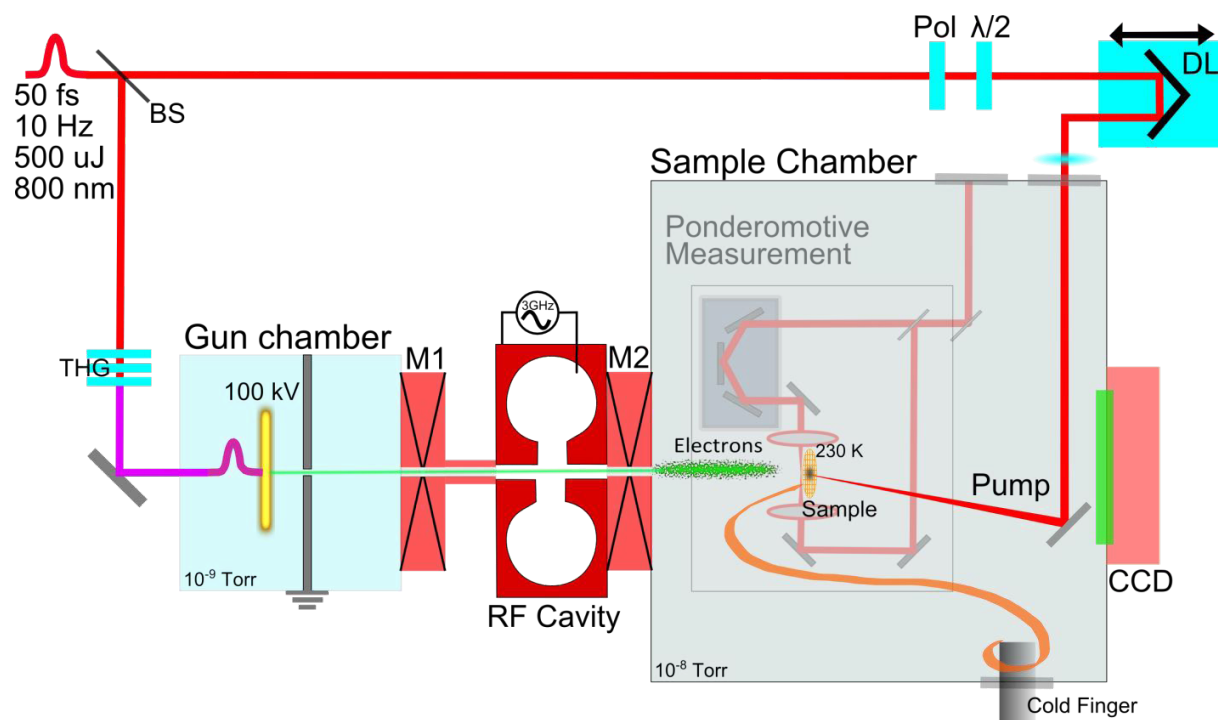


Fig.S1: Layout of our ultrabright femtosecond electron diffraction (FED) setup showing the hybrid RF-DC electron gun and the geometrical arrangement for pulse duration measurements (light grey background) and pump configuration relevant to FED experiments. The sample is represented as a grey spot on the yellow mesh.

## 2. Experimental Conditions

We used electron bunches of 40 fC each with a spot size of  $(280 \pm 20)$   $\mu\text{m}$  FWHM at the sample position. The measured Gaussian IRF is  $(430 \pm 75)$  fs FWHM. The experiment was conducted with a repetition rate of 10 Hz. The diffraction pattern was recorded on a phosphor-coated, low noise fiber-coupled CCD capable of single electron detection. The background vacuum pressure was  $1 \times 10^{-8}$  mbar. The sample was mounted on a standard copper TEM grid and placed in a homebuilt liquid nitrogen cold finger assembly. The equilibrium temperature of the sample was measured to be  $(230 \pm 5)$  K with a calibrated thermo-resistor. For optical excitation in the second charge transfer (CT2) band<sup>33,34</sup>, we use the direct output of our Ti-Sapphire amplifier at a central wavelength of 800 nm. At the sample position, the pulse energy was  $(2.0 \pm 0.05)$   $\mu\text{J}$ , the spot size  $(400 \pm 20)$   $\mu\text{m}$  FWHM and, the pump pulse duration  $(60 \pm 5)$  fs FWHM. The polarization was linear and chosen to be along the direction of the stacking axis of the EDO-TTF molecules, i.e. that of the transition dipole moment of the CT2 band. The incident excitation fluence was  $2.2 \times 10^{15}$  photons/ $\text{cm}^2$  or  $0.55$  mJ/ $\text{cm}^2$ . To recover the absorption depth, we directly measured the transmission of the pump pulse through the sample to be  $(66 \pm 2)$  % at 230 K (and  $(93 \pm 2)$  % at 295 K). The combination of the transmission with the reflectivity data (10 % at 800 nm at near normal incidence) provides an excitation density of  $7 \times 10^{19}$  photons/ $\text{cm}^3$  or 0.08 photons per low temperature unit cell.

## 3. Data Collection and Processing

The data displayed in Fig. S2 were the average of at least 10 runs. Each diffraction image was collected with an exposure time of 5 seconds at 10 Hz (50 pulses). Each trace comprised 5 images per time point. The time traces were repeated 10 times, making a cumulative average of

2,500 pulses per time point. Each time trace was collected in approximately 1.5 hours. Every pump-on shot was followed by a pump-off shot. A “pump scatter” image was also collected for every time trace, where the electron beam was blocked but the optical beam was allowed to hit the sample. This allowed unwanted pump scatter light to be subtracted from the pump-on images.

After data collection, we post-processed the images by: a) correcting for slow spatial electron beam drift by re-centering each diffraction pattern. The center for each image was found taking the average bisector of at least 3 peak pairs ( $hkl$ ) and  $-(hkl)$ ; and b) removing the diffuse electron scattering background. Fig. S2a shows a typical averaged diffraction pattern. Fig. S2b shows the inelastic scattering background obtained from radial averaging, and Fig. S2c shows the result of the subtraction.

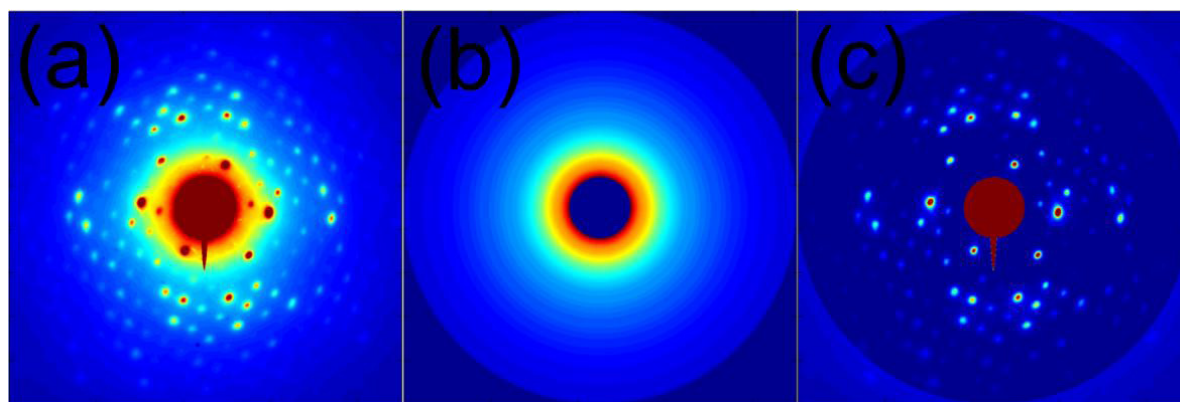


Fig.S2: **a** original diffraction pattern of LT state. **b** diffuse background. **c** after background removal.

For the interest of measuring changes in lattice parameters, we would like to have both small spot sizes (transfer width) at the screen and low centroid noise. The latter is limited by the transverse electron beam stability. Fig. S3 compares the average experimental peak widths, centroid noise, and measurable peak

shifts. From this we see that the difference in peak positions from the HT to the LT states are easily discernible but peak shifts from transient states with only a small converted fraction of unit cells are not resolvable with the current signal-to-noise level.

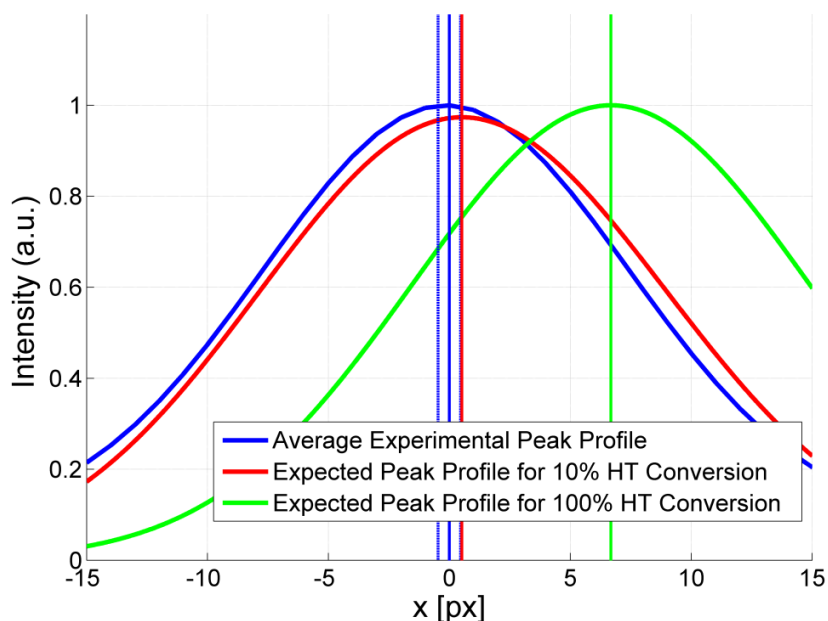


Fig.S3. The blue trace represents the averaged experimental peak profile for the (542) peak. The red curve represents the expected peak shift for 10% of the LT unit cells converted to the HT state. The green curve represents the expected peak shift for 100% conversion to the HT state. The solid lines represent the centroid of these curves while the dotted blue lines represent the experimental centroid noise due to beam pointing instability. This implies that for 10% conversion, the peak shift is unlikely to be resolved with a reasonable degree of certainty in our experiment.

## 4. Control Experiments

### 4.1 Polarization Dependence

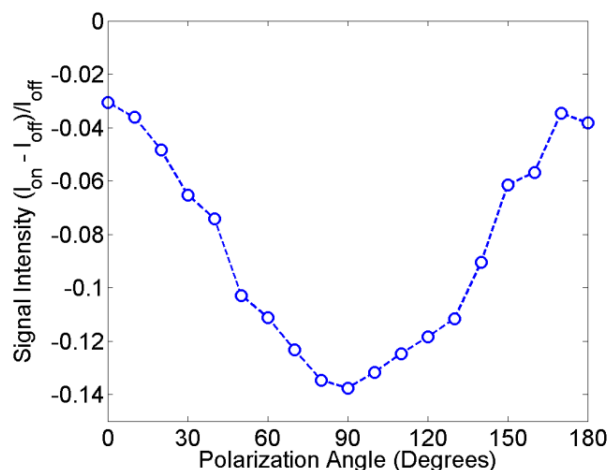


Fig. S4: Relative intensity changes for the (-4 -3 -2) peak as a function of the relative angle between the (fixed) sample and the direction of the polarization of the pump. The time delay was set at 100 ps.

We performed several control experiments to check the validity of our results. The first obvious check was polarization dependence of the time resolved signal. The absorption via the CT2 band should reach a maximum when the polarization is tuned along the stacking axis of EDO-TTF molecules and nearly disappear when tuned in the perpendicular direction. Figure S4 shows the amplitude of the relative intensity changes for the (-4 -3 -2) peak (at a time delay of 100 ps) versus the relative angle between the sample and the polarization of the pump pulse. This behaviour illustrates the structural changes are specifically related to electronic excitation via the CT2 band.

## 4.2 Fluence Dependence

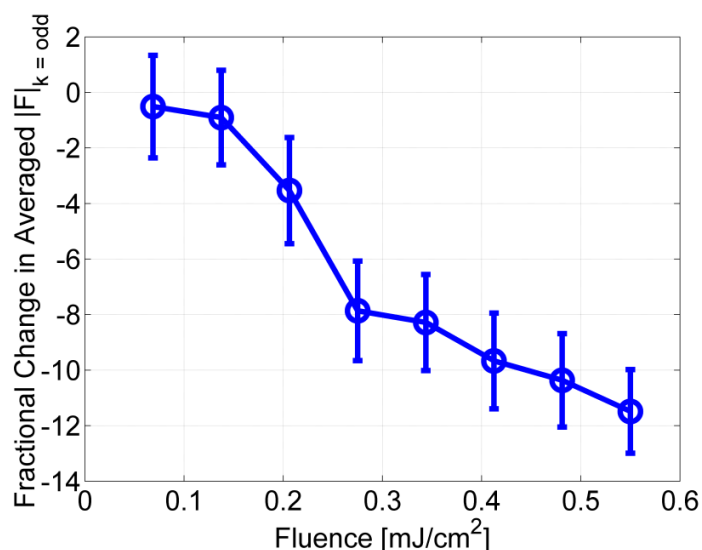


Fig. S5: Fluence dependence of the fractional change in the averaged structure factor amplitude for  $(h\ k\ l)$  reflections with  $k = \text{odd}$  values. The time delay was set at +1 ns. Error bars represent the standard deviation.

We recorded fluence dependent measurements for a fixed time delay of +1 ns for excitations from 0.07 mJ/cm<sup>2</sup> ( $2.7 \times 10^{14}$  photons/cm<sup>2</sup>) to 0.55 mJ/cm<sup>2</sup> ( $2.2 \times 10^{15}$  photons/cm<sup>2</sup>). We did not attempt to exceed 0.55 mJ/cm<sup>2</sup> as it was very close to the damage threshold (due to peak power) and we had a very limited supply of high quality samples. Fig. S5 shows the structure factor amplitude averaged over all visible  $(h\ k\ l)$ -reflections with  $k = \text{odd}$  values (i.e., reflections that do not exist in the HT phase) as a function of the incident fluence. Although a threshold-like behavior (near  $F = 0.2$  mJ/cm<sup>2</sup>) seems to be evident, making a substantial inference about the shape of the trace requires a better signal-to-noise ratio and it goes beyond the scope of this work.

### 4.3 Accumulated Heating

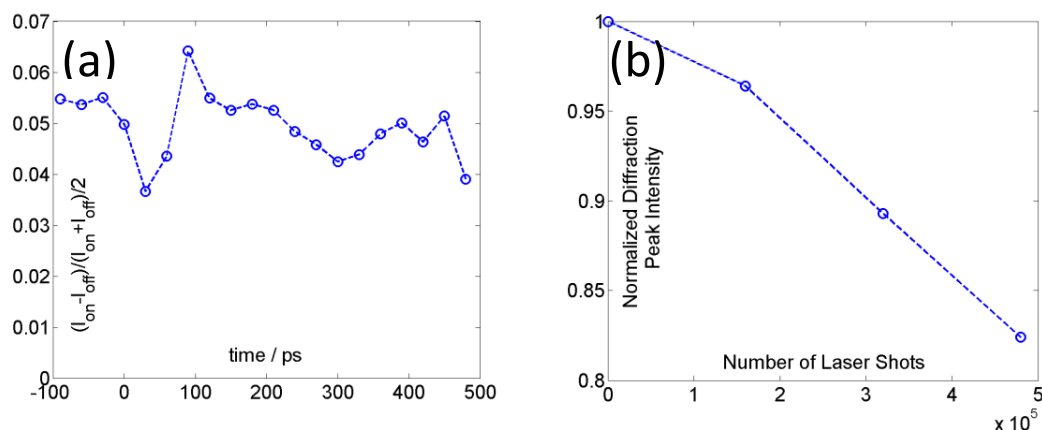


Fig.S6: **a** Normalized differential diffraction intensity of a reflection when pumped at 1 kHz. The non-zero signal before  $t_0$  implies that there are significant accumulated heating effects. **b** The intensity of the same reflection decreases rapidly with the number of pump shots indicating sample damage. The incident fluence used was  $\sim 1 \text{ mJ/cm}^2$ .

We also carefully ruled out the effects of accumulated heating in our data. Fig. S6a shows a time trace from experiments performed at a repetition rate of 1 kHz instead of 10 Hz, using the same excitation energy per pulse. A strong signal is seen before time zero, meaning the heat deposited by a laser shot does not fully dissipate before the next shot arrives. Fig. S6b shows the steady decrease of the absolute diffracted intensity as the number of shots increase (at a repetition rate of 1 kHz). This is indicative of sample damage. The experiment was also attempted at 100 Hz and an appreciable signal could not be measured before raising the pulse energy above the onset of accumulated heating/sample damage. This feature to the experiment is quite important as it is likely that the sample is primarily cooled by black body radiation (poor conduction) and further highlights the importance of using high density electron bunches for ultrafast diffraction. The



experiment requires a certain fraction of the unit cells to be excited and an unavoidable associated change in lattice temperature when the system has relaxed. High repetition sampling methods would not have worked as illustrated in Fig.S6 since we could not observe the dynamics even at repetition rates as low as 100 Hz. The ability to obtain sufficient signal above the noise level at data collection rates of 10 Hz was only possible with this newly developed high intensity electron source.

## 5. Sample Preparation

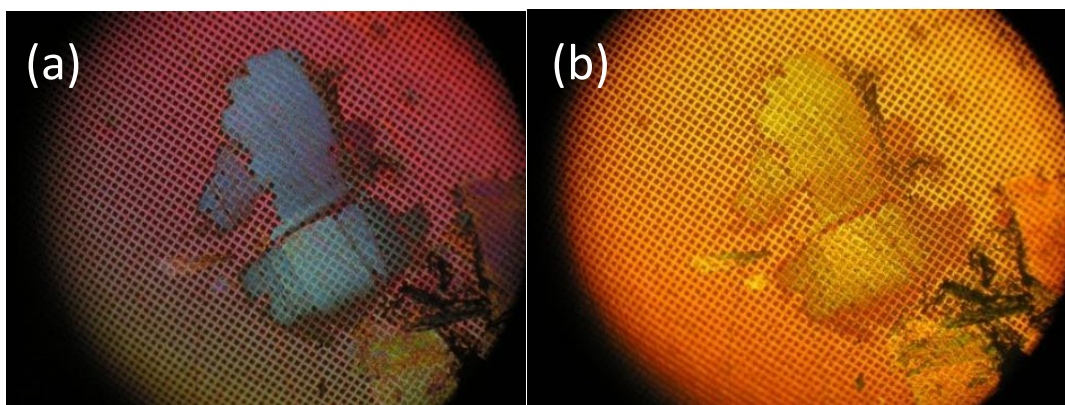


Fig.S7. **a** Microscope image of a 100 nm thick slice of  $(\text{EDO-TTF})_2\text{PF}_6$  for the a polarization orthogonal to the stacking axis. **b** Polarization parallel to the stacking axis.

The quasi-1D organic salt,  $(\text{EDO-TTF})_2\text{PF}_6$  is well suited for cleavage by ultra-microtomy to thicknesses in 100-nm range which is optimal for organic materials to be studied by electron diffraction (FED) in transmission mode at 100 kV. The  $(\text{EDO-TTF})_2\text{PF}_6$  single crystals were grown by the electron-crystallization method<sup>35</sup> and then cleaved roughly parallel to the a-b plane. The section size was typically  $500\ \mu\text{m} \times 500\ \mu\text{m} \times 100\ \text{nm}$ . The samples were picked up from the water surface using standard TEM copper grids with different supporting membranes. Fig.S7 shows a typical microtomed  $(\text{EDO-TTF})_2\text{PF}_6$  sample on a TEM grid under a polarization

microscope. The contrast between the sample and the background is distinctly different for polarization along the stacking axis (Fig.S7a) and polarization perpendicular to the stacking axis (Fig.S7b).

## 6. Data Analysis

### 6.1 Change of basis (unit cell)

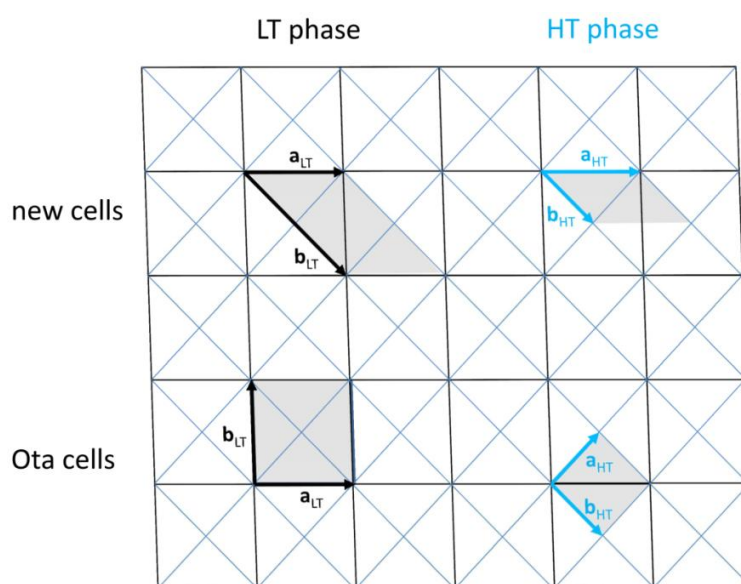


Fig. S8: The conversion schematic between the equivalent Ota unit cells (bottom) and the common cells (top) used in the data analysis. The c-axis remains unchanged for the HT phase and is reversed for the LT phase.

The HT and the LT phases are triclinic and centro-symmetric (space group P-1). The transition from HT to LT involves a (almost) doubling of the unit cell along the stacking direction of the EDO-TTF molecules. For practical reasons to this study, we redefined the unit cells derived from the Ota work<sup>35</sup> such that both phases have approximately the same cell constants and angles, except that the b axis of the LT cell which is nearly twice the b axis of the HT cell. The relations

between the new and the original unit cells are:  $\mathbf{a}_{\text{new}}^{\text{HT}} = \mathbf{a}_{\text{ota}}^{\text{HT}} + \mathbf{b}_{\text{ota}}^{\text{HT}}$ ,  $\mathbf{b}_{\text{new}}^{\text{HT}} = \mathbf{b}_{\text{ota}}^{\text{HT}}$ ,  $\mathbf{c}_{\text{new}}^{\text{HT}} = \mathbf{c}_{\text{ota}}^{\text{HT}}$  for the HT phase;  $\mathbf{a}_{\text{new}}^{\text{LT}} = \mathbf{a}_{\text{ota}}^{\text{LT}}$ ,  $\mathbf{b}_{\text{new}}^{\text{LT}} = \mathbf{a}_{\text{ota}}^{\text{LT}} - \mathbf{b}_{\text{ota}}^{\text{LT}}$ ,  $\mathbf{c}_{\text{new}}^{\text{LT}} = -\mathbf{c}_{\text{ota}}^{\text{LT}}$  for the LT phase.

Figure S8 demonstrates this relationship in the a-b plane. All the analysis and indexing in this manuscript refers to these unit cell parameters. The cell parameters used are as follows:

HT phase:  $a = 9.597 \text{ \AA}$ ,  $b = 7.343 \text{ \AA}$ ,  $c = 11.948 \text{ \AA}$ ,  $\alpha = 93.42^\circ$ ,  $\beta = 81.58^\circ$ ,  $\gamma = 48.05^\circ$

LT phase:  $a = 9.822 \text{ \AA}$ ,  $b = 14.803 \text{ \AA}$ ,  $c = 11.487 \text{ \AA}$ ,  $\alpha = 92.72^\circ$ ,  $\beta = 80.87^\circ$ ,  $\gamma = 47.99^\circ$

## 6.2 Symmetry Changes

The symmetry changes outlined in section 6.1 are reflected in the experimental diffraction patterns as well. The most obvious difference between the LT and HT diffraction patterns (as seen in Fig. 1 in the main text) is the disappearance of all the odd rows of peaks, indicative of cell doubling. In terms of the new cell parameters (S 6.1), the peaks with indices  $(h, k, l)$  where  $k = \text{odd}$  values disappear. However, in the transient data, this is more complicated. We would also like to point out to the reader that it is not at all obvious to assume that the HT-like state in the transient data possess the same symmetry and/or lattice parameters as the HT state. Additional information from the precise determination of the peak positions may answer this point, but it requires further improvements of our FED setup. However we can infer that the symmetry changes approaches that of the HT state on the 1 ns time scale by looking at the evolution of reflections with  $k = \text{odd}$  values. Fig. S9 shows the time-dependent structure factor amplitude averaged over all reflections with  $k = \text{odd}$  values. Under the assumption that in the HT-type state  $k = \text{odd}$  reflections are very close to zero, the 10 % drop in structure factor amplitude between  $t = 0$  and  $t = 1 \text{ ns}$  agrees with the estimation of eq. S5 for the fraction of LT unit cells converted to the HT-type state.

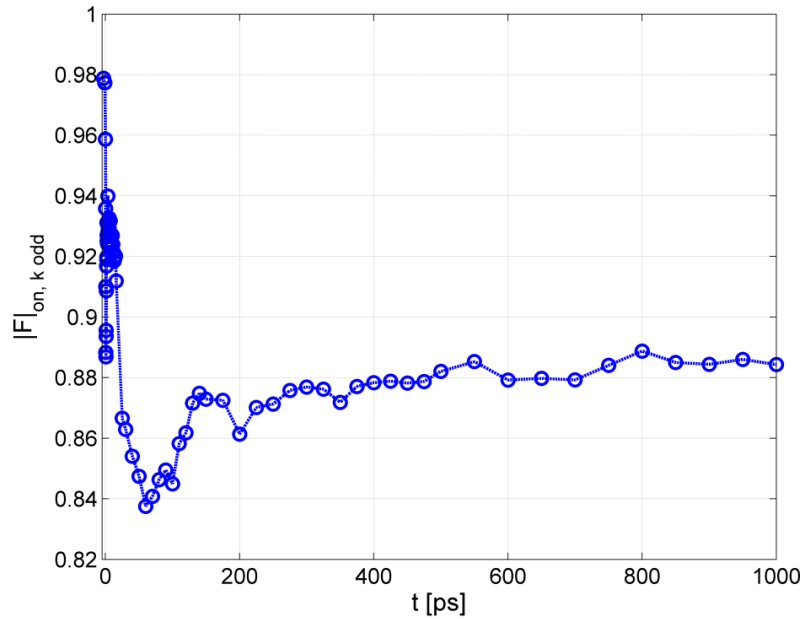


Fig. S9: Structure factor amplitude averaged for  $(h\ k\ l)$ -reflections with  $k = \text{odd}$  values. This is indicative of partial recovery of the symmetry of the HT state at 1 ns.

### 6.3 Kinematical Electron Diffraction Simulations

For this study, we used the kinematic theory for electron diffraction to simulate the experimental diffraction patterns. To justify the use of kinematical theory over dynamical theory, we need to evaluate whether or not the sample thickness for the electron beam conditions lies within the weak-phase-object approximation (WPO):

The condition for the WPO can be expressed as<sup>36</sup>:

$$\varepsilon = \left| \frac{t\lambda F(\mathbf{k})}{\Omega} \right|, \varepsilon \ll 1 \quad (\text{S1})$$

Where  $t, \lambda, F, \Omega$  are respectively the crystal thickness, electron wavelength, structure factor, and unit cell volume.

In the current study, these parameters have values of:

$$t = 10^3 \text{ \AA}$$

$$\lambda = 0.036 \text{ \AA}$$

$$\Omega = 1198.1 \text{ \AA}^3$$

$$F = 2.23 \text{ \AA}$$

where  $F$  is taken to be the median of simulated structure factor magnitude for  $k \leq 1.5 \text{ \AA}^{-1}$ . For these values,  $\varepsilon = 0.07$ ; therefore, it is reasonable to employ the single scattering formulation for electron diffraction:

$$F(\mathbf{k}) = \sum_{j=1}^N f_j(\mathbf{k}) e^{2\pi i \mathbf{k} \cdot \mathbf{r}_j} \quad (\text{S2})$$

Where  $f_j$  is the atomic scattering factor for the  $j^{\text{th}}$  atom, parameterized as<sup>37</sup>:

$$f_j(k) = \sum_{l=1}^5 a_l e^{\frac{1}{4} b_l k^2} \quad (\text{S3})$$

## 6.4 Orientation determination

There are inherent uncertainties in the alignment of the sample. We determined the observed orientation of the sample by finding a best fit of the LT and HT diffraction patterns.

An automatic procedure was set up, which can predict *for any arbitrary orientation* the partial intensities that would appear in the vicinity of the observed spots, taking into account the finite width of the relrods (reciprocal lattice points extended by convolution with a shape function). Then, this algorithm was used to find an optimum orientation of the crystal which minimizes the

differences between the predicted and the measured intensities. This procedure does not require any presupposition about the Miller indices of the spots.

The profile of the relrods was described as a convolution of the shape function (effect of the finite size of the crystal, same for all spots) and a Gaussian function representing the combined effect of mosaicity and beam divergence (rms width  $\sigma_{mb}$  proportional to  $s = \sin \theta / \lambda$ ,  $\sigma_{mb} = as$ ). To reduce the computational load, the shape function (which for a thin crystal slab would be a sinc function) was also approximated by a Gaussian function ( $\sigma_{sh} = b$ ) so that the combined profile again is Gaussian with standard deviation  $\sigma = \sqrt{(as)^2 + b^2}$ , parameters  $a$  and  $b$  being treated as fit parameters.

In total, the least squares procedure included 6 fit parameters: the parameters  $a$  and  $b$  for the profile of the relrods, a constant factor  $K$  and an isotropic B-factor ( $B_{iso}$ ) for overall scaling of the intensities, and two parameters,  $u$  and  $v$ , determining the orientation of the crystal. [ $u, v, w = 1$ ] are the fractional coordinates of a vector parallel to  $\mathbf{k}_0$  (wave vector of the incident beam) relative to the unit cell axes ( $u = v = 0$  would correspond to the [001] zone axis). The optimum orientations for HT and LT were determined independently (best values [ $uvw$ ] = [-0.675, 0.60, 1] for HT, [-0.64, 0.266, 1] for LT; note that the ratio of the  $v$  values is close to 2, which is consistent with the cell doubling). The angles between these directions and the  $c$  axes ([001] directions) are 23.9° (HT) and 23.6° (LT). Fig.S10 illustrates these vectors.

The two crystal orientations agree within about 1°, if both unit cells are referred to the same standard Cartesian coordinate system ( $x \parallel \mathbf{a}$ ;  $z \perp (\mathbf{a} \text{ and } \mathbf{b})$ ). Part of the 1° angular deviation between the two orientations may be caused by the difference in the unit cell parameters between LT and HT which probably results in a slight rotation of the Cartesian coordinate system relative

to the laboratory system. The beam direction relative to the crystal structure is shown in Fig.S10. The R factors for the best orientation were 40.8% and 35.2% for the HT and the LT phases, respectively ( $R = \sum |F_{\text{calc}} - F_{\text{obs}}| / \sum |F_{\text{obs}}|$ , with  $F = \sqrt{I}$ , all reflections included). Figs.S11 **a, b** show the experimental HT and LT diffraction patterns (schematically, with the areas of the spots being proportional to the structure factor amplitudes). Figs.S11**c, d** show the simulated spot intensities for the optimized orientation, and Figs.S11**e, f** show the overlay of the observed spots with all reflections contributing to the spot intensities at their expected positions.

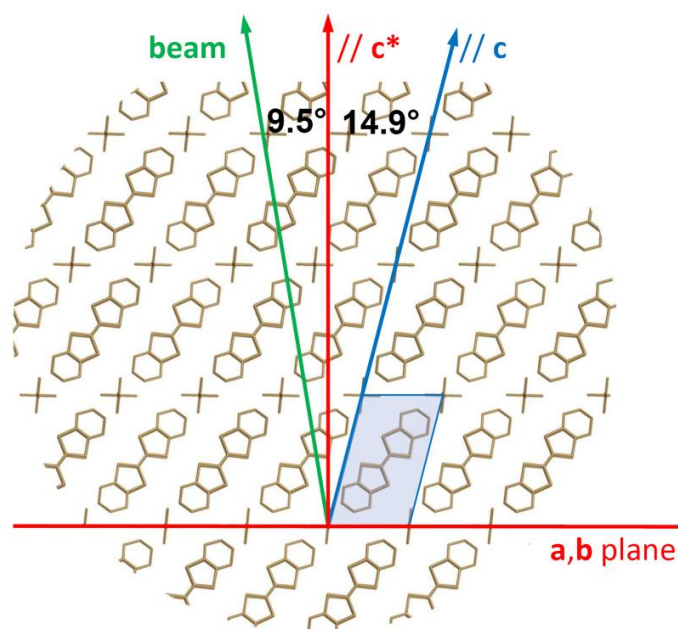


Fig. S10: Illustration showing the relative angles between the electron beam direction, the [001] zone axis and the axis perpendicular to the a-b plane (cleavage plane of the sample).

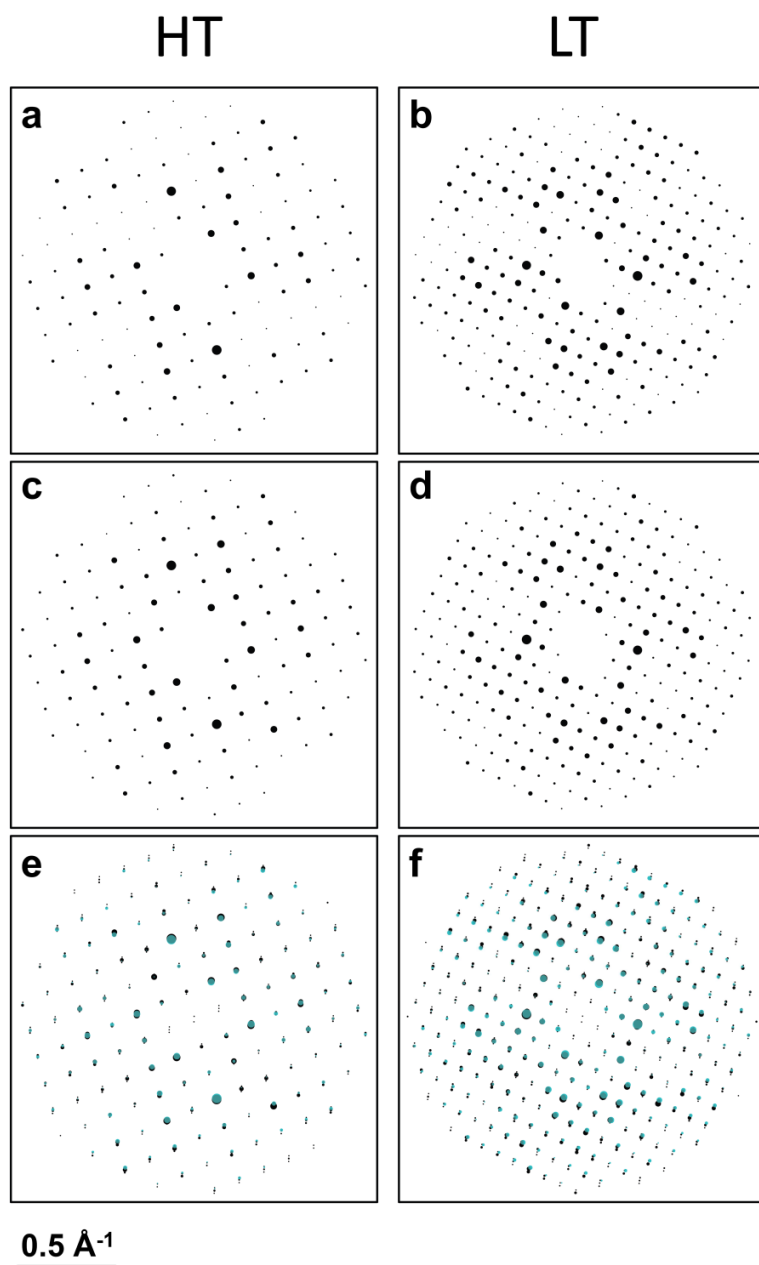


Fig. S11: **a** and **b** shows the replotted HT and LT diffraction patterns where the spot areas are proportional to the structure factor amplitudes. **c** and **d** shows the diffraction pattern for the optimal simulated orientations. **e** and **f** shows the overlay of the observed spots (as in **a**, **b**) with the individual intensity contributions (cyan) at their predicted positions.



## 7 Time dependent model, Correlation function, and Optimization

We explicitly treated the experimental case where the pump pulse excites a small fraction of the sample, which then evolves from the initial LT state, whose diffraction pattern can be described with the structure factors  $F_{\text{LT}}$ , and eventually converts into the final HT state with structure factors,  $F_{\text{HT}}$ . At the relatively low excitation used, we assume the excited molecules are randomly distributed within the crystal lattice and any clustering would be within the coherence region of the probing electron pulse. Employing a solution for solving time-resolved crystallography proposed by Coppens *et al.*<sup>38</sup>, the observed structure factor amplitude of the pumped crystal  $F_{\text{exp}}(\mathbf{k}, t)$  can be written as a sum of that of the initial state  $F_{\text{LT}}$  and the excited state  $F_{\text{exc}}$ , weighted by the excitation fraction  $\eta_{\text{exc}}$ :

$$|F_{\text{exp}}(\mathbf{k}, t)| = |\eta_{\text{exc}} F_{\text{exc}}(\mathbf{k}, t) + (1 - \eta_{\text{exc}}) F_{\text{LT}}(\mathbf{k})| \quad (\text{S4})$$

By inverting the above equation and using measurements at late times, a value for  $\eta_{\text{exc}}$  is found:

$$\eta_{\text{exc}} = \frac{F_{\text{exp}}(\mathbf{k}, t_{\infty}) - F_{\text{LT}}(\mathbf{k})}{F_{\text{HT}}(\mathbf{k}) - F_{\text{LT}}(\mathbf{k})} \quad (\text{S5})$$

Judging from the experimental data, we assume the system has reached a stationary state by 1 ns so we take  $t_{\infty} \approx 1 \text{ ns}$ . Due to the rational form of this equation and its resulting sensitivity to noise, a distributed set of values  $\eta_{\text{exc}}(\mathbf{k})$  is expected. By eliminating those peaks whose reciprocal lattice points are far away from the Ewald sphere, we reduced the data to a set of approximately 40 peaks with the relevant time-resolved data to reconstruct the molecular

motions. Fig.S12 shows the calculated excitation fractions for these peaks, a normal distribution with mean  $\eta_{\text{exc}} = 0.103 \pm 0.008$ . The amplitude component of the structure factors from the static LT and HT images were extracted by first integrating the pixel values in a circular region around the peaks and then taking the square root.

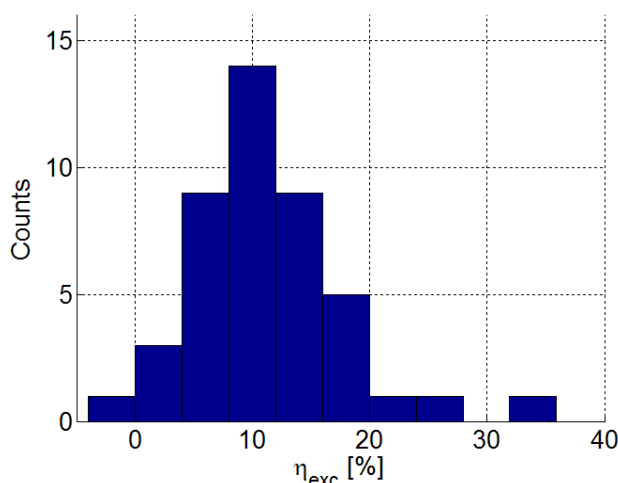


Fig. S12: The distribution of excited fraction of LT unit cells calculated for a subset of 40 peaks using eq. S5. The distribution is centered around  $\eta_{\text{exc}} = 10\%$ . The time delay was 1 ns.

Given the initial LT and final HT structures, the simplest model one can use to extract the key atomic motions is a linear interpolation between the two. Fig. 3 in the main text illustrates the atomic displacement linking the initial LT and final HT-type structures. Fig.S13 shows a stereo-plot of the molecular displacements that map the molecule from the LT to the HT state. It follows naturally to construct a time dependent model to separate the three moieties with three distinct center of mass motions: the motion of the flat EDO-TTF molecules (F) mostly characterized by sliding, the unbending of the bent EDO-TTF molecules (B), and displacement of the counter ions  $\text{PF}_6$  (P). In this model, the 3 moieties are allowed to evolve independently (in time) from their LT to their HT coordinates, but in a linear fashion. This leads to the construction of a finite 3-dimensional reaction coordinate space where each point in the space represents a

possible intermediate structure. For each time point measured in the experimental data, we can find the point in this configuration space that best matches the measured diffraction and construct the entire reaction pathway.

This model works under several underlying assumptions that cannot be overlooked: a) the fraction of molecules undergoing the transition from LT to HT remains constant b) the reaction dynamics is coherent and homogenous in nature c) inversion symmetry is preserved at all times.

a) If the fraction of molecules changes during the observed time scales, we would expect that the final fraction of converted molecules is significantly different from the initial excited fraction. However, we estimated the excited fraction to be  $\sim 8\%$  (Section 2), and at  $t = 1$  ns, the estimate of the converted fraction from the structure factor amplitudes was  $\sim 10\%$ . In addition, during the model calculations, we obtained independently that the correlation coefficient only drops if we assume anything other than 10% excited fraction (this is shown in Fig. S15). These observations suggest that the photo-induced phase transition involves a roughly constant fraction of molecules evolving from the LT to the HT-type state.

b) It is not known a priori whether the reaction proceeds in a homogenous manner; that is all the molecules are moving in a similar fashion and are synchronized. This is a fair assumption for the observed fast dynamics in the 0-10 ps temporal window where molecular motions can be considered to be coherent; an argument that is valid for the determination of the TIS (Transient Intermediate Structure). This observation is also consistent with optical measurements<sup>33,34</sup> that show clear evidence (in the few ps range) of the existence of a well peaked spectrum that does

not resemble either the LT state or the HT state. The timescales are in good agreement with those observed in our diffraction experiments and support the fact that our diffraction data in the TIS region must reflect that of a special intermediate structure. However, it is important to mention that the slow dynamics, in the 100 ps range, reflect uncorrelated motions characteristic of a thermal process and, therefore, refinement calculations would provide an ensemble-averaged structure. In optical data the spectrum evolves towards that of a metallic-type state.

The present study is focused on the fast dynamical component and the determination of the TIS since for longer time delays (as explained in the manuscript) the diffraction signal is contaminated by acoustic wave effects.

c) The model preserves the center of symmetric, i.e. motions are centro-symmetric. Although at the single unit cell level this is not necessarily true. This is justified in this case. Since the LT unit cell is centro-symmetric and the excitation field as well then, the overall change observed in our diffraction data is centro-symmetric. Our electron probe averages over many unit cells and optical photoexcitation from an initial ground ( $D^{+1}D^{+0}D^{+0}D^{+1}$ ) leads to ( $D^{+1}D^{+0}D^{+1}D^{+0}$ ) and ( $D^{+0}D^{+1}D^{+0}D^{+1}$ ) electronic excited states with equal probability.

Below there is a formal description of this method.

First we define the 3 moieties in the LT unit cell:

- 1) B group: the two initially bent EDO-TTF molecules; undergoes unbending motion towards HT

- 2) F group: the two initially flat EDO-TTF molecules; undergoes mostly a sliding motion towards the HT state
- 3) P group: the two  $\text{PF}_6$  anions

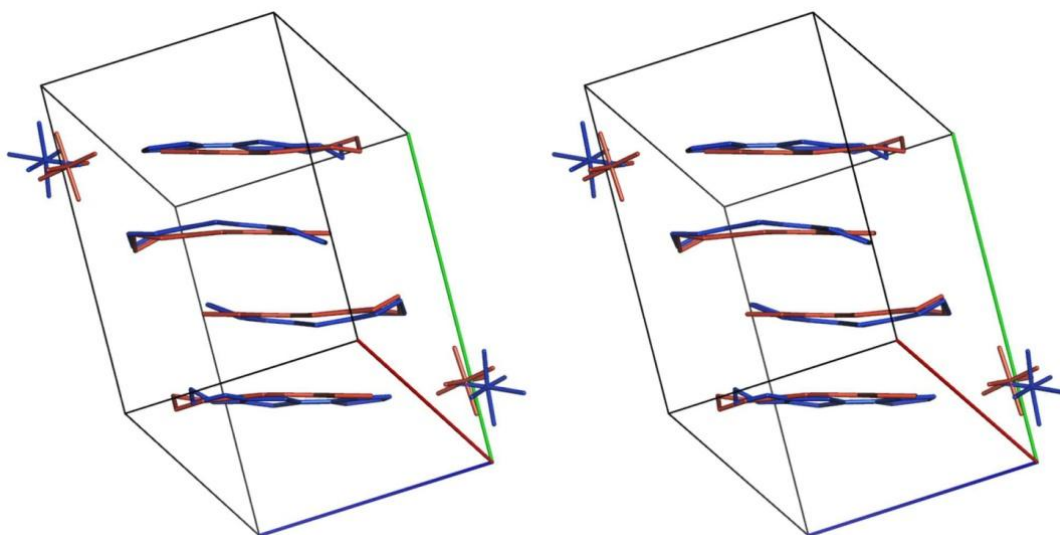


Fig.S13: Stereo-plot of the overlay between the LT (blue) and the HT (red) molecular coordinates with the atomic displacements from HT to LT exaggerated by a factor of 2.

The 3 associated reaction coordinates,  $\xi_g$  with  $g = B, F, P$ , are defined by assuming a linear interpolation for atomic motions:

$$\mathbf{R}_{\text{exc},g}(t) = \xi_g(t) * (\mathbf{R}_{\text{HT},g} - \mathbf{R}_{\text{LT},g}) + \mathbf{R}_{\text{LT},g} \quad (\text{S6})$$

Where  $\mathbf{R}_{\text{exc},g}$ ,  $\mathbf{R}_{\text{LT},g}$ ,  $\mathbf{R}_{\text{HT},g}$  are the coordinates of the atoms within each dynamic group  $g$ . Thus, the triplet specifies a point  $\xi = (\xi_B, \xi_F, \xi_P)$  in this reduced configuration space where:

- 1) LT state:  $(\xi_B, \xi_F, \xi_P) = (0,0,0)$
- 2) HT state:  $(\xi_B, \xi_F, \xi_P) = (1,1,1)$

The region of configuration space  $(\xi_B, \xi_F, \xi_P)$  that contains the expected points of interest is considered ( $\xi_g \in [-2.0, 2.0]$ ) and was sampled with a step of ( $\Delta\xi_g = 0.01$ ). For every grid point, an excited state structure is defined by Eq. S6; its associated set of observable structure factor amplitudes  $|F_{\text{sim,exc}}(\mathbf{k}, \xi)|$  is calculated and linearly mixed with that from the LT state,  $|F_{\text{sim,LT}}(\mathbf{k})|$  as before:

$$|F_{\text{sim,exc}}(\mathbf{k}, \xi_B, \xi_F, \xi_P)| = |\eta_{\text{exc}} F_{\text{sim,exc}}(\mathbf{k}, \xi_B, \xi_F, \xi_P) + (1 - \eta_{\text{exc}}) F_{\text{sim,LT}}(\mathbf{k})| \quad (\text{S7})$$

We used the Pearson coefficient for the measure of the goodness of fit between two diffraction patterns:

$$\gamma(F_1, F_2) = \frac{\sum_{\mathbf{k}} c_1(\mathbf{k}) c_2(\mathbf{k})}{\sqrt{\sum_{\mathbf{k}} c_1(\mathbf{k})^2} \sqrt{\sum_{\mathbf{k}} c_2(\mathbf{k})^2}} \quad (\text{S8})$$

$$c_i(\mathbf{k}) = \frac{F_i(\mathbf{k}) - \bar{F}_i}{\bar{F}_i}$$

$$\bar{F}_i = \frac{\sum_{\mathbf{k}} F_i(\mathbf{k})}{N}$$

The strategy for structure reconstruction is to compute and maximize the correlation between the experimental structure factor amplitudes,  $|F_{\text{exp}}(\mathbf{k}, t)|$ , and the simulated ones,  $|F_{\text{sim}}(\mathbf{k}, \xi)|$ , for every time delay. Thus, the problem is distilled down to a search for the global maximum in the function  $\Gamma(\xi, t) = \gamma(|F_{\text{exp}}(\mathbf{k}, t)|, |F_{\text{sim}}(\mathbf{k}, \xi)|)$  using  $\eta_{\text{exc}} \equiv 10\%$ . Fig.S15 shows that if we choose a different  $\eta_{\text{exc}}$ , then the correlation drops, providing an independent check for this model.

Fig. S14 shows the solution for  $\Gamma(\xi, t = 0 \text{ ps})$  (Here 0 ps refers to just before the onset of optical excitation; it is also equivalent to any negative time delay points) displayed using a 3D isosurface plot in configuration space, with a cut-off at 95% of its maximum value and perpendicular contour planes. The solution is very well behaved and clearly shows only one maximum very close to the expected (0,0,0) point, matching the LT structure. The optimal solution is well behaved for all time points (see animation in supplementary media files), evolves towards the HT state (1,1,1), is always positive, and traces a nearly smooth trajectory with no smoothing in time applied to the experimental data. The trajectory of the solutions for all time points is displayed in Figs. 3 **b** and **c** in the main text.

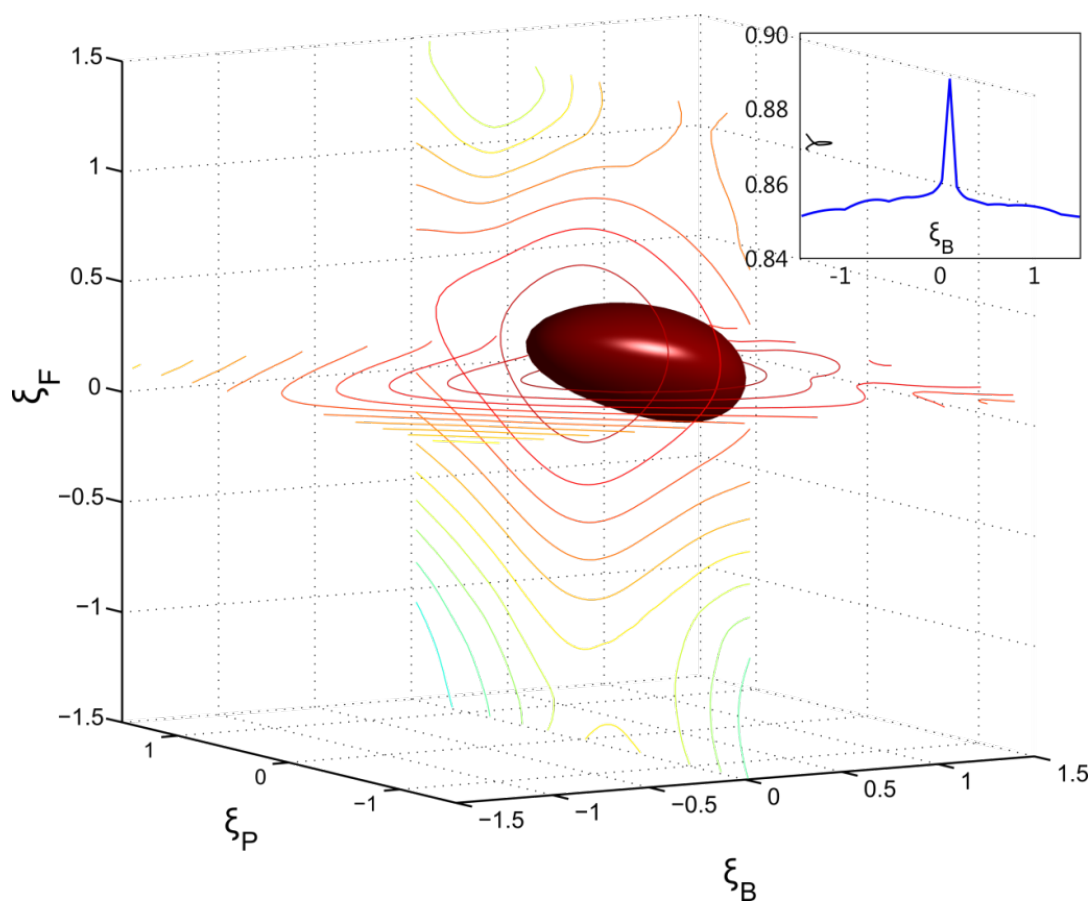


Fig. S14: 3D isosurface plot of  $\Gamma(\xi, t = 0 \text{ ps})$  with intensity cut-off at 95%. The solution is clearly peaked around (0,0,0) Corresponding to the LT state of the system. The inset shows a 1D cross-section of the main figure, again showing that the maximum is very sharply peaked. The FWHM of this peak is used to quote an error bound in Fig S16 and Fig 3c in the manuscript.

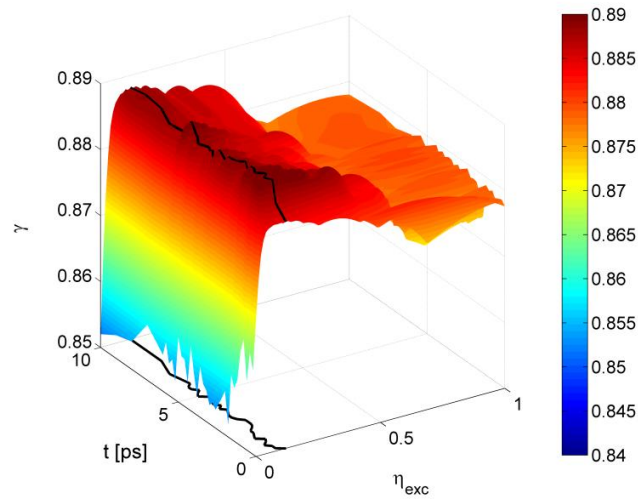


Fig. S15: The calculation for  $\Gamma(\xi, t = 0 \rightarrow 10 \text{ ps})$  using different values for  $\eta_{\text{exc}}$ . The correlation peaks at approximately 10% for all time delays, providing further evidence for an excited fraction of LT unit cells of ~10%

We fitted the 3 components of the trajectory to a four exponential decay model  $f(t)$ :

$$\begin{aligned}
 A(t) &= A_0 \left( e^{-t/\tau_2} - e^{-t/\tau_1} \right) H(t) \\
 B(t) &= B_0 \left( e^{-t/\tau_4} - e^{-t/\tau_3} \right) H(t) \\
 R(t) &= G_\sigma(t) \\
 f(t) &= R(t) * (A(t) + B(t)) \quad (\text{S9})
 \end{aligned}$$



Where  $H(t)$  is the Heaviside function,  $R(t)$  is the instrument response function (modelled as a Gaussian function  $G_\sigma(t)$  with  $\sigma = 430$  fs), and  $f(t)$  is the fitting function. The fitting model makes no assumptions about the physics of the temporal trajectory, but only serves to quantify the time scales of the reactions. Constants  $\tau_1$  and  $\tau_2$  describes the early fast rise and decay;  $\tau_3$  and  $\tau_4$  characterize the transient intermediate state. The optimized structures with projections along the key reaction coordinates were individually fitted as a function of time delay using the above functions for each coordinate ( $\xi_B, \xi_S, \xi_P$ ). Table S1 describes the resulting fitting parameters.

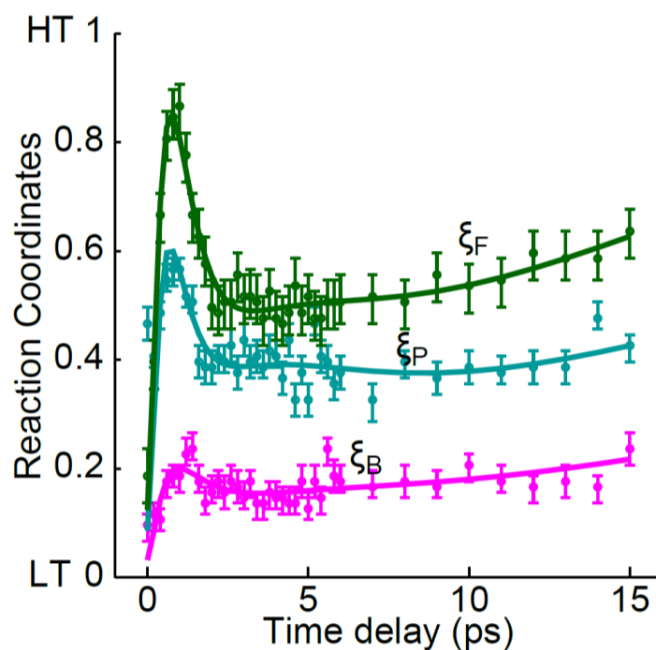


Fig. S16: Evolution of reaction coordinates in the formation of the TIS. Solid curves were obtained through exponential fitting using Eq. S9 for  $\xi_g(t)$ . Error bars represent the FWHM of the global maximum peaks of the Pearson correlation coefficient in reaction coordinate space (see inset in Fig. S14).

	$A_0$	$B_0$	$C_0$	$\tau_1[\text{ps}]$	$\tau_2[\text{ps}]$	$\tau_3[\text{ps}]$	$\tau_4[\text{ps}]$	$R^2$
$\xi_B$	15.3 $\pm 0.6$	6.9 $\pm 0.8$	1.46 $\pm 0.09$	0.7 $\pm 0.1$	0.7 $\pm 0.1$	3.4 $\pm 0.6$	3.6 $\pm 0.7$	0.978
$\xi_F$	56 $\pm 1$	1.0 $\pm 0.1$	0.95 $\pm 0.04$	0.49 $\pm 0.05$	0.53 $\pm 0.06$	2.8 $\pm 0.3$	3.2 $\pm 0.8$	0.840
$\xi_P$	32 $\pm 1$	6.0 $\pm 0.7$	1.23 $\pm 0.04$	0.44 $\pm 0.07$	0.45 $\pm 0.06$	2.0 $\pm 0.5$	4.3 $\pm 0.5$	0.971

Table S1: Table of fitting parameters with errors corresponding to Eq. S9. The errors represent the standard error of the fit.

### Appendix 1 - Atomic Coordinates used in Model Calculations

Atom		LT			TIS (t = +5 ps)			HT		
		x	y	z	x	y	z	x	y	z
6	C1	14.39755	8.52445	5.26772	14.24036	8.51690	5.17947	14.04823	8.50767	5.07162
6	C2	15.28781	8.17499	6.26248	15.10019	8.20722	6.20196	14.87087	8.24661	6.12799
6	C3	13.19361	8.84983	3.07080	13.12123	8.82061	2.93575	13.03278	8.78489	2.77068
6	C4	17.23137	7.16415	7.55668	17.01877	7.27514	7.58915	16.75893	7.41079	7.62885
6	C5	12.45310	9.50724	3.98128	12.36869	9.51538	3.80330	12.26552	9.52533	3.58577
6	C6	16.49637	7.81222	8.45940	16.25952	7.95985	8.44464	15.97003	8.14028	8.42661
6	C7	11.51024	9.20503	1.50490	11.49972	9.23722	1.29729	11.48685	9.27655	1.04354
6	C8	11.12171	10.35932	2.25236	11.12221	10.38543	2.04817	11.12282	10.41735	1.79859
16	S1	14.63081	8.06100	3.62374	14.50895	7.99581	3.55397	14.36002	7.91613	3.46870
16	S2	16.69564	7.22847	5.93001	16.51809	7.24978	5.94855	16.30108	7.27584	5.97121
16	S3	12.99035	9.46244	5.62159	12.83062	9.48070	5.46606	12.63539	9.50301	5.27596
16	S4	15.08603	8.64346	7.90357	14.85484	8.74585	7.82114	14.57227	8.87098	7.72040
8	O1	12.90977	8.77991	1.74888	12.88246	8.73768	1.60552	12.84909	8.68606	1.43030
8	O2	11.30912	10.16928	3.70958	11.25946	10.21277	3.47774	11.19878	10.26592	3.19439
6	C9	12.57795	5.66887	6.01850	12.54645	5.65145	6.01847	12.41219	5.57719	6.01831
6	C10	11.76655	5.86335	4.96163	11.73292	5.85858	4.96169	11.58955	5.83825	4.96194
6	C11	13.56634	5.40557	8.35182	13.53999	5.38551	8.34563	13.42764	5.29997	8.31924
6	C12	9.77511	6.36580	3.43233	9.76112	6.42437	3.43779	9.70150	6.67406	3.46108

6	C13	14.34139	4.66680	7.56444	14.31356	4.64642	7.55299	14.19490	4.55953	7.50416
6	C14	10.59300	5.64934	2.69485	10.57350	5.70543	2.68886	10.49039	5.94457	2.66331
6	C15	14.46156	4.35440	10.17833	14.44618	4.34177	10.17498	14.38061	4.28792	10.16068
6	C16	15.66735	4.13710	9.36988	15.66070	4.13495	9.34969	15.63236	4.12577	9.26363
16	S5	12.26919	6.32243	7.61656	12.23712	6.29323	7.61745	12.10040	6.16873	7.62123
16	S6	10.27542	6.78432	5.04625	10.25337	6.78902	5.06002	10.15934	6.80902	5.11872
16	S7	14.04478	4.71090	5.84317	14.00303	4.68638	5.83762	13.82503	4.58184	5.81396
16	S8	12.11345	5.17822	3.38720	12.07065	5.18500	3.38384	11.88815	5.21388	3.36953
8	O3	13.68611	5.47009	9.70923	13.67190	5.45655	9.69981	13.61133	5.39879	9.65962
8	O4	15.37279	3.87929	7.98031	15.35167	3.86782	7.96420	15.26164	3.81893	7.89554
15	P1	17.39163	8.43106	0.23744	17.29181	8.37932	0.04213	17.15395	8.30786	-0.22757
9	F1	16.29411	9.56272	0.37928	16.16222	9.44855	0.14428	15.98010	9.29088	-0.18023
9	F2	18.49886	7.31776	0.13308	18.42702	7.32074	-0.03827	18.32780	7.32485	-0.27490
9	F3	17.65083	8.47665	1.83982	17.42291	8.28864	1.59994	17.10816	8.02901	1.26867
9	F4	17.10796	8.46948	-1.26425	17.14650	8.51872	-1.45727	17.19973	8.58671	-1.72381
9	F5	18.60297	9.45985	0.06876	18.40778	9.45876	0.01267	18.13823	9.45726	-0.06478
9	F6	16.19058	7.45596	0.50459	16.18179	7.33102	0.12871	16.16967	7.15847	-0.39035
6	C1	7.15421	0.09921	5.82221	7.31140	0.10676	5.91046	7.50353	0.11599	6.01831
6	C2	6.26396	0.44867	4.82745	6.45157	0.41644	4.88797	6.68089	0.37705	4.96194
6	C3	8.35815	-0.22617	8.01913	8.43053	-0.19695	8.15418	8.51898	-0.16123	8.31924
6	C4	4.32039	1.45951	3.53325	4.53299	1.34852	3.50077	4.79283	1.21287	3.46108
6	C5	9.09866	-0.88358	7.10864	9.18307	-0.89172	7.28663	9.28624	-0.90167	7.50416
6	C6	5.05539	0.81144	2.63053	5.29224	0.66381	2.64528	5.58173	0.48337	2.66331
6	C7	10.04152	-0.58137	9.58502	10.05204	-0.61356	9.79264	10.06491	-0.65289	10.04638
6	C8	10.43005	-1.73566	8.83756	10.42955	-1.76177	9.04176	10.42894	-1.79369	9.29134
16	S1	6.92095	0.56266	7.46618	7.04281	0.62785	7.53595	7.19174	0.70753	7.62123
16	S2	4.85612	1.39519	5.15992	5.03367	1.37387	5.14138	5.25068	1.34782	5.11872
16	S3	8.56141	-0.83878	5.46833	8.72114	-0.85704	5.62387	8.91637	-0.87936	5.81396
16	S4	6.46573	-0.01980	3.18636	6.69692	-0.12219	3.26878	6.97949	-0.24732	3.36953
8	O1	8.64199	-0.15625	9.34105	8.66930	-0.11402	9.48441	8.70267	-0.06240	9.65962
8	O2	10.24264	-1.54562	7.38035	10.29230	-1.58911	7.61218	10.35298	-1.64226	7.89554
6	C9	8.97382	2.95478	5.07142	9.00531	2.97221	5.07146	9.13957	3.04647	5.07162
6	C10	9.78521	2.76031	6.12829	9.81884	2.76508	6.12824	9.96221	2.78541	6.12799
6	C11	7.98542	3.21809	2.73810	8.01177	3.23815	2.74429	8.12412	3.32369	2.77068
6	C12	11.77665	2.25786	7.65759	11.79064	2.19929	7.65213	11.85026	1.94959	7.62885
6	C13	7.21037	3.95686	3.52549	7.23820	3.97724	3.53694	7.35686	4.06413	3.58577
6	C14	10.95876	2.97432	8.39507	10.97826	2.91822	8.40107	11.06137	2.67909	8.42661
6	C15	7.09020	4.26926	0.91159	7.10558	4.28189	0.91495	7.17115	4.33574	0.92925
6	C16	5.88441	4.48656	1.72005	5.89106	4.48871	1.74024	5.91941	4.49789	1.82630
16	S5	9.28257	2.30122	3.47337	9.31464	2.33043	3.47248	9.45136	2.45493	3.46870
16	S6	11.27634	1.83933	6.04368	11.29839	1.83464	6.02991	11.39242	1.81464	5.97121
16	S7	7.50698	3.91275	5.24676	7.54873	3.93728	5.25230	7.72673	4.04182	5.27596
16	S8	9.43831	3.44544	7.70273	9.48111	3.43866	7.70609	9.66361	3.40978	7.72040

8	O3	7.86565	3.15356	1.38070	7.87986	3.16711	1.39012	7.94043	3.22486	1.43030
8	O4	6.17897	4.74437	3.10962	6.20009	4.75584	3.12572	6.29012	4.80472	3.19439
15	P1	4.16013	0.19260	10.85249	4.25996	0.24434	11.04779	4.39781	0.31579	11.31750
9	F1	5.25765	-0.93907	10.71065	5.38954	-0.82489	10.94565	5.57167	-0.66722	11.27016
9	F2	3.05290	1.30590	10.95685	3.12474	1.30292	11.12820	3.22396	1.29881	11.36483
9	F3	3.90093	0.14701	9.25011	4.12885	0.33501	9.48999	4.44360	0.59464	9.82126
9	F4	4.44380	0.15418	12.35418	4.40526	0.10494	12.54719	4.35203	0.03694	12.81374
9	F5	2.94879	-0.83619	11.02117	3.14398	-0.83510	11.07726	3.41353	-0.83360	11.15471
9	F6	5.36118	1.16770	10.58534	5.36997	1.29264	10.96121	5.38209	1.46519	11.48028

Table S2: Table of 70 atomic positions within one unit cell for the LT, the transient intermediate structure (calculated at  $t = +5$  ps), and the HT-type structure used for interpolation (here the HT unit cell was doubled in size to match the LT unit cell). All values are given in Cartesian coordinates (in Angstroms) where the X-axis is parallel to the b-axis of the LT unit cell.

## References

- <sup>31</sup> Gao, M., *et al.*, Full characterization of RF compressed femtosecond electron pulses using ponderomotive scattering. *Opt. Express* **20**, 12048-12058 (2012).
- <sup>32</sup> Hebeisen, C. T., *et al.*, Grating enhanced ponderomotive scattering for visualization and full characterization of femtosecond electron pulses. *Opt. Express* **16**, 3334-3341 (2008).
- <sup>33</sup> Onda, K., *et al.*, Photoinduced Change in the Charge Order Pattern in the Quarter-Filled Organic Conductor (EDO-TTF)<sub>2</sub>PF<sub>6</sub> with a Strong Electron-Phonon Interaction. *Phys. Rev. Lett.* **101**, 067403 (2008).
- <sup>34</sup> Fukazawa, N., *et al.*, Charge and structural dynamics in photoinduced phase transition of (EDO-TTF)<sub>2</sub>PF<sub>6</sub> examined by picosecond time-resolved vibrational spectroscopy. *J. Phys. Chem. C* **116**, 5892-5899 (2012).
- <sup>35</sup> Ota, A., Yamochi, H. & Saito, G., A novel metal-insulator phase transition observed in (EDO-TTF)<sub>2</sub>PF<sub>6</sub>. *J. Mat. Chem.* **12** (2002).
- <sup>36</sup> Zou, X., Hovmoller, S., Oleynikov, P., *Electron Crystallography – Electron Microscopy and Electron Diffraction, IUCr Texts on Crystallography, Vol. 16, Oxford University Press, 2011.*

- 
- <sup>37</sup> Peng, L.-M., Ren, G., Dudarev, S. L. & Whelan, M. J., Robust parameterization of elastic and absorptive electron atomic scattering factors. *Acta. Cryst. A* **52**, 257–276, (1996).
- <sup>38</sup> Coppens, P., Vorontsov, I. I., Graber, T., Gembicky, M. & Kovalevsky, A.Y., The structure of short-lived excited states of molecular complexes by time-resolved X-ray. *Acta Cryst. A* **61**, 162–172 (2005).